Geometric-Frequency Operating-Quantity Extraction for Distance and Directional Protection in Converter-Dominated Power Systems

Jinhui Chen, *Student Member, IEEE,* Huadong Sun, *Senior Member, IEEE,* Shiyun Xu, *Senior Member, IEEE,* Bing Zhao, *Senior Member, IEEE,* Congbo Wang, and Federico Milano, *Fellow, IEEE*

***Abstract*—In converter-dominated grids, the earliest post-fault interval is often limited by operating-quantity extraction, because cycle-based discrete Fourier transform (DFT) phasors can incur finite-window bias under fast control actions, current limiting, and waveform distortion. This paper develops a trajectory-based, sub-cycle operating-quantity extractor that acts directly on instantaneous three-phase measurements. Leveraging the recently proposed concept of geometric frequency (GF) and using short-window least-squares differentiation, the proposed method separates the instantaneous stretching and rotation of the three-phase trajectory and converts them into a closed-form equivalent series R–L drop. Resulting parameters are mapped onto the conventional R–X plane to drive standard mho and quadrilateral logic. A memory-polarized directional torque is also formed from instantaneous three-phase vectors to maintain sign consistency under voltage depression while reducing cycle-length reporting latency. Electromagnetic transient (EMT) case studies on a wind-farm export corridor and real-time digital simulator (RTDS)-based validation on a modified IEEE 9-bus transmission system verify the effectiveness of the proposed GF-based distance and directional protection method.**

***Index Terms*—Geometric frequency, converter-dominated power systems, distance protection, directional protection, time-domain protection, non-sinusoidal conditions.**

I. Notation

In this paper, scalars are indicated by italic lower-case letters (e.g., t) and vectors by bold lower-case letters (e.g., $\boldsymbol{u}$). The operator $\|\cdot\|$ denotes the Euclidean norm, $(\cdot)^\top$ the transpose, and $(\cdot)^*$ the complex conjugate.

A. Scalars

- t: time (s).
- T_s, f_s: sampling period and sampling frequency, $f_s = 1/T_s$.
- f_0, ω_0: nominal frequency (Hz) and angular frequency, $\omega_0 = 2\pi f_0$.
- N: samples per nominal cycle, $N = f_s/f_0$.
- $\mathcal{W}_n$: short-window index set for GF estimation and windowed averaging.
- R_ℓ, L_ℓ: total series resistance and inductance of the protected line (per phase).
- m: fault location factor.
- R_f: fault resistance (Ω).
- R_d, L_d: equivalent parameters identified from waveforms in the single-ended formulation.

B. Vectors and signals

- $\boldsymbol{u}(t) \in \mathbb{R}^3$: three-phase vector signal.
- $\boldsymbol{v}(t)$, $\boldsymbol{\imath}(t)$: local three-phase voltage and current.
- $\boldsymbol{u}'(t)$: time derivative of $\boldsymbol{u}(t)$.
- $\boldsymbol{v}_{\rm mem}$: memory (prefault) polarizing voltage vector.
- $\Delta\boldsymbol{\imath}$: superimposed (incremental) current, $\Delta\boldsymbol{\imath} = \boldsymbol{\imath} - \boldsymbol{\imath}_{\rm prefault}$.
- $\hat{\boldsymbol{n}}_{\rm mem}$: hemisphere-locked memory axis (unit vector) used for GF directional projection.

C. GF descriptors and operators

- $\rho_u(t)$: stretching rate (radial frequency).
- $\boldsymbol{\omega}_u(t)$: angular frequency vector.
- $\omega_u(t)$: angular frequency magnitude, $\omega_u = \|\boldsymbol{\omega}_u\|$.
- $\tilde{\boldsymbol{\Gamma}}_u(t)$: GF operator, $\boldsymbol{u}' = \tilde{\boldsymbol{\Gamma}}_u \boldsymbol{u}$ with $\tilde{\boldsymbol{\Gamma}}_u = \rho_u + \boldsymbol{\omega}_u \times$.

II. Introduction

A. Motivation

DISTANCE and directional elements remain the core primitives of transmission and sub-transmission line protection. In mainstream practice, these functions are implemented with cycle-based phasor estimation, most commonly via the DFT, and conventional impedance- or torque-comparator logic, as summarized in classical relaying references [1]. Many conventional relay implementations are designed around quasi-sinusoidal operating quantities and reporting windows in which the underlying quantities are expected to be approximately stationary within the estimator [2]. Even with synchronized measurements and two-ended formulations, operating quantities can inherit finite-window bias whenever the waveform evolves appreciably within the reporting window [3].

Converter-dominated operation and weak-grid conditions stress these assumptions in the first post-fault tens of milliseconds, which increasingly determine protection speed and dependability. Protection reports [4], [5] document that inverter-based resources (IBRs) can depress fault current,

This work was supported in part by the Sustainable Energy Authority of Ireland (SEAI) under project FRESLIPS, Grant No. RDD/00681. *(Corresponding author: Huadong Sun.)*

J. Chen, H. Sun, S. Xu, B. Zhao, and C. Wang are with the China National Key Laboratory of Power Grid Security, China Electric Power Research Institute, Beijing 100192, China (e-mail: chenjh_cepri@163.com; sunhd@epri.sgcc.com.cn; xushiyun@epri.sgcc.com.cn; zhaobing@epri.sgcc.com.cn; wangcongbo107@163.com).

F. Milano is with the School of Electrical and Electronic Engineering, University College Dublin, Dublin D04 V1W8, Ireland (e-mail: federico.milano@ucd.ie).

reshape sequence behavior, and introduce control-driven nonstationarity that makes cycle-based quantities slower to settle. System-operator guidance and field-event studies further show that such responses may include low-magnitude and time-varying IBR fault currents, harmonic, interharmonic, and fast-transient components, distorted relay input signals, distance-relay misoperation, memory-polarized logic issues, and directional-element misoperation risks [6]–[8]. These characteristics can distort apparent impedance, weaken faulted-phase selection and sequence-based supervision, and challenge memory-polarized directional logic during fast transients, thereby increasing the risk of incorrect tripping, delayed operation, or undesired blocking in conventional phasor-based protection [9], [10].

For many line-protection functions, the decision logic is mature, while the early-time operating quantities remain the limiting factor. Under fast distortion and control-driven nonstationarity, phasor-based quantities may lose their direct correspondence with instantaneous voltage-current behavior. Complex-frequency and geometric-frequency viewpoints provide a trajectory-based way to describe such dynamics without requiring steady-state phasors [11]–[14]. Building on this idea, this paper develops GF-based sub-cycle operating quantities that retain zero-sequence and unbalanced components while feeding standard relay comparators.

B. Related Work and Research Gap

Recent studies on transmission-line protection have pursued faster and more robust operation under converter-dominated conditions and waveform distortion.

Existing protection studies related to this work can be grouped into four representative streams according to the source of the protection operating quantity and the way in which converter-dominated fault behavior is addressed.

First, enhanced phasor-estimation methods improve the extraction of fundamental-frequency quantities from distorted protection signals. Improved DFT-based algorithms suppress decaying dc offsets, harmonics, and noise in protection signal extraction [15], [16]. Other modified DFT-based algorithms further improve phasor estimation for numerical relaying applications under decaying dc offsets, harmonics, noise, and related transient disturbances [17], [18]. These methods improve phasor convergence under selected signal disturbances, while still following a windowed fundamental-frequency representation. When IBR controls reshape the waveform within the estimation window, the extracted phasor may include finite-window bias.

Second, IBR-adapted phasor-based distance and directional protection methods modify impedance calculation, relay logic, phase-comparator implementation, reactance measurement, or converter-control coordination to address low-magnitude, limited, and control-dependent fault-current behavior. Representative studies include control-based fault-current regulation, mitigation strategies for IBR-related line-protection challenges, and practical phase-comparator and reactance-method implementations [19]–[21]. Recent studies further analyze distance-protection behavior under grid-forming inverter current limiting [22] and improve compatibility with different inverter control schemes using local phasor and sequence-network information [23]. These methods are important for IBR-connected lines and provide practical adaptations of conventional relay principles. Their performance, however, may be influenced by the assumed converter behavior when fault currents are highly distorted, time-varying, or strongly control-dependent.

Third, transient-feature and traveling-wave protection methods use fault-generated high-frequency components for fast fault discrimination. A protection perspective in [24] argues that phasor-window latency is not fundamental and discusses the associated speed–security tradeoffs for faster line elements. Traveling-wave schemes provide a very fast time-domain alternative, and recent studies have further exploited wavefront or first-arrival information for power-electronic-device-interfaced ac and dc line protection [25], [26]. Their performance may depend on measurement bandwidth, wavefront identification, propagation-time setting, reflection interpretation, sensor response, and fault inception conditions [27], [28]. Under attenuated traveling-wave signatures, complex reflections, or limited voltage-sensor bandwidth, the extraction of wavefront information may become more demanding.

Fourth, incremental-quantity and practical time-domain protection methods construct operating quantities from fault-generated voltage-current changes. Practical time-domain relays use incremental quantities and traveling waves for high-speed elements and require settings related to incremental levels and traveling-wave propagation times [29]. Incremental-quantity directional and distance elements have also been developed from instantaneous voltage-current relations [30], [31]. These methods improve speed and provide practical time-domain alternatives to conventional phasor-based elements. Their performance can depend on prefault references, filtering windows, short-time fault-network approximations, transformed-frame construction, and practical time-domain settings. When converter controls reshape post-fault currents or current limiting changes the equivalent source behavior, the incremental relation may require additional care in interpretation.

In parallel, geometric representations have matured into implementable and circuit-consistent tools. Applications of the Frenet frame [32] show that three-phase trajectory geometry can provide measurable electrical observables. However, translating geometric descriptors into relay-grade operating quantities for distance and directional protection remains insufficiently explored.

The research gap with respect to existing representative protection methods is summarized in Table I.

This paper addresses this gap by providing a geometry-consistent operating-quantity extraction stage that directly extracts relay-ready quantities from instantaneous three-phase trajectories, without phasor reconstruction, sequence decomposition, or wavefront identification. The extracted quantities can be directly used by standard distance characteristics and directional torque comparators.

TABLE I
SUMMARY OF REPRESENTATIVE PROTECTION METHODS AND POSITIONING OF THE PROPOSED GF METHOD

Factor	Enhanced phasor estimation	IBR-adapted phasor-based protection	Transient-feature and traveling-wave protection	Incremental-quantity and time-domain protection	Proposed GF method
Refs.	[15]–[18]	[19]–[23]	[24]–[28]	[29]–[31]	This paper
Basic quantity	Fundamental phasor	Phasor, sequence component, apparent impedance, comparator, or control-related quantity	Transient feature or traveling-wave quantity	Incremental voltage-current quantity	GF stretching and rotation
Main dependence	Data window for phasor estimation	IBR fault-current behavior, converter control, and relay implementation	Wavefront detection, propagation time, reflection pattern, or high-frequency transient feature	Prefault reference, incremental quantity, filtering, or time-domain setting	Instantaneous three-phase trajectory
Physical meaning	Sinusoidal fitting	Impedance, sequence-network, phase-comparator, reactance, or control-related relay relation	Transient propagation and wavefront behavior	Short-time incremental fault-network relation	Resistive and inductive stretching or rotational relation
Three-phase modeling	Phase or sequence based	Phase-loop, sequence-network, or converter-control-model based	Modal or fault-loop traveling-wave quantity based	Loop, modal, or transformed-frame incremental quantity based	Unified abc instantaneous modeling including unbalanced and zero-sequence components
Relay compatibility	Direct for conventional phasor-based relays	Direct or implementation dependent	Method dependent	Method dependent	Directly mapped to distance and directional logic
Main role / consideration	Improves phasor convergence; finite-window effects may remain during fast waveform changes	Adapts phasor-based relay logic to IBR-connected lines; performance may depend on phasor, sequence, control, or converter assumptions	Enables fast transient-based protection; performance may depend on sensing bandwidth, wavefront extraction, and reflection interpretation	Provides practical time-domain quantities; performance may depend on incremental reference, filtering, or short-time model	Provides relay-ready sub-cycle quantities without phasor reconstruction, sequence decomposition, or wavefront identification

C. Contributions

This paper proposes a geometric-frequency operating-quantity extraction framework for converter-dominated systems. Specific contributions are as follows.

- A clarification on why cycle-based DFT operating quantities can be biased in the first post-fault interval under fast controls, current limiting, and waveform distortion, and how these biases propagate into distance and directional elements.
- A short-window two-ended extractor that estimates fault location and fault resistance from synchronized instantaneous three-phase measurements, without full-cycle phasor reporting.
- A short-window single-ended extractor that estimates distance and fault resistance from local instantaneous three-phase measurements, enabling communication-free deployment.
- A technique to map the extracted quantities to the conventional impedance plane so standard mho and quadrilateral logic can be used without changing decision characteristics.
- An instantaneous-vector directional supervision with practical polarization selection, using instantaneous voltage when reliable and memory polarization under voltage depression, with a locked reference axis to preserve sign consistency.

EMT-based case studies on a wind-farm export corridor verify faster settling and improved stability of operating quantities compared with DFT-based implementations under stressed conditions. RTDS tests on a modified IEEE 9-bus transmission system further demonstrate the real-time implementation feasibility and relay compatibility of the proposed GF-based distance and directional elements.

D. Paper Organization

Section III summarizes conventional DFT-based distance and directional elements and highlights finite-window bias mechanisms under non-sinusoidal conditions. Section IV introduces the geometric-frequency framework and derives the operating quantities used for distance and directional elements for both single-ended and two-ended implementations. Section V presents EMT case studies and comparative results. Section VI presents RTDS-based real-time experimental validation on a modified IEEE 9-bus transmission system. Section VII draws conclusions and outlines future work.

III. Phasor-Based Protection and Error Sources

A. Sliding-Window DFT Phasors and Finite-Window Bias

Consider a real-valued signal $x(t)$ sampled at period T_s, with $x[n] = x(nT_s)$. Let the nominal system frequency be f_0 and define the number of samples per nominal cycle as

$$N = \frac{f_s}{f_0}, \qquad f_s = \frac{1}{T_s}. \tag{1}$$

The one-cycle sliding-window DFT phasor estimate of the nominal-frequency fundamental at discrete time n is

$$\hat{X}[n] = \frac{2}{N}\sum_{k=0}^{N-1} x[n-k]\mathrm{e}^{-j\frac{2\pi}{N}(n-k)}. \tag{2}$$

For protection implementations, (2) is commonly realized in a recursive form:

$$\hat{X}[n] = \hat{X}[n-1] + \frac{2}{N}\Big(x[n] - x[n-N]\Big)\mathrm{e}^{-j\frac{2\pi}{N}n}. \tag{3}$$

The key observation is that (2) relies on near-orthogonality inside the finite window, which is only guaranteed when the waveform is approximately stationary and quasi-sinusoidal over one cycle. In the first post-fault cycles, fast control actions, current limiting, and nonstationary transients typically violate this assumption, yielding a time-varying bias in $\hat{X}[n]$.

A generic decomposition of the sampled signal is

$$x[n] = x_{\text{fund}}[n] + x_{\text{dc}}[n] + x_{\text{harm}}[n], \tag{4}$$

where $x_{\text{fund}}[n]$ is the fundamental component, $x_{\text{dc}}[n]$ is the dc offset, and $x_{\text{harm}}[n]$ collects all remaining non-fundamental components.

Substituting (4) into (2) yields

$$\hat{X}[n] = X_1[n] + E_{\text{dc}}[n] + E_{\text{harm}}[n], \tag{5}$$

where $X_1[n]$ is the desired nominal-frequency fundamental phasor, and $E_{\text{dc}}[n]$ and $E_{\text{harm}}[n]$ are time-varying bias terms induced by finite-window non-orthogonality and leakage.

Fig. 1 illustrates the bias mechanism in (5). Fig. 1(a) shows that, within a one-cycle sliding window, the DFT projection enforces a nominal-frequency sinusoid fit that cannot perfectly match a nonstationary post-fault waveform. Fig. 1(b) visualizes the resulting phasor geometry: the estimate $\hat{X}$ can be interpreted as the vector sum of the true fundamental component X_1 and the bias phasors. Fig. 1(c) reports the time evolution of these bias magnitudes, emphasizing the early transient interval.

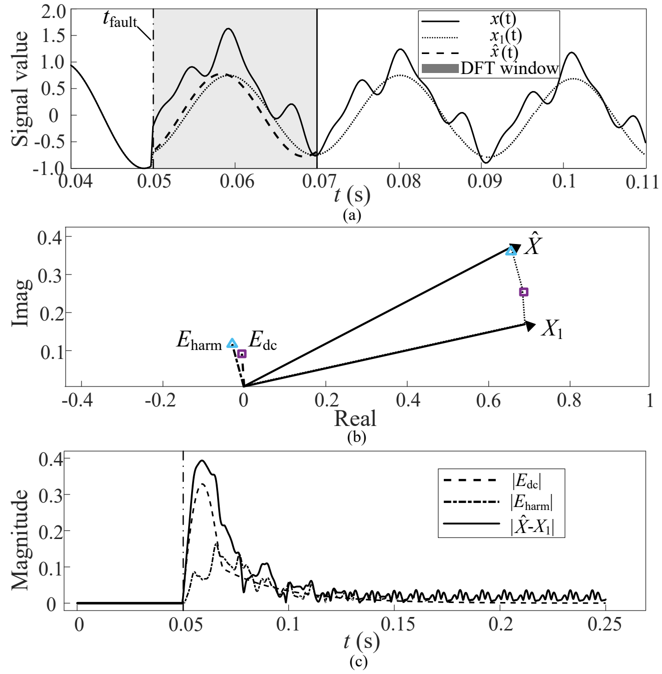

Fig. 1. Finite-window DFT bias mechanism: (a) one-cycle sliding window and nominal-frequency fit on a nonstationary waveform; (b) geometric illustration of how bias accumulates in the estimated phasor; (c) time evolution of the bias magnitude in the early transient interval.

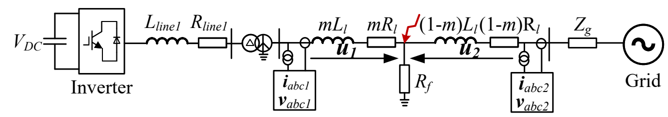

Fig. 2. Two-ended fault loop model.

B. Two-Ended Phasor Distance Protection Mechanism

Fig. 2 shows the two-ended fault-loop model of a protected line. The fault is located at a normalized distance $m \in [0, 1]$ from terminal 1 with fault resistance R_f. Here, $m = 0$ and $m = 1$ correspond to terminal 1 and terminal 2, respectively.

Under a lumped series model without shunt capacitance, the phasor KVL equations are

$$\begin{aligned} \hat{V}_{1,\phi}[n] &= \hat{V}_{f,\phi}[n] + m\, Z_\ell\, \hat{I}_{1,\phi}[n], \\ \hat{V}_{2,\phi}[n] &= \hat{V}_{f,\phi}[n] + (1-m)\, Z_\ell\, \hat{I}_{2,\phi}[n], \end{aligned} \tag{6}$$

where $\hat{V}_{1,\phi}$, $\hat{V}_{2,\phi}$ and $\hat{I}_{1,\phi}$, $\hat{I}_{2,\phi}$ are the terminal voltage and current phasors measured at terminals 1 and 2, respectively. The terminal currents are defined positive from each terminal toward the protected line, $\hat{V}_{f,\phi}$ is the fault-point voltage phasor, Z_ℓ is the total series impedance of the protected line, and ϕ denotes the selected faulted phase.

Eliminating $\hat{V}_{f,\phi}[n]$ yields the conventional two-ended distance estimate

$$\hat{m}_\phi[n] = \frac{\hat{V}_{1,\phi}[n] - \hat{V}_{2,\phi}[n] + Z_\ell\, \hat{I}_{2,\phi}[n]}{Z_\ell\big(\hat{I}_{1,\phi}[n] + \hat{I}_{2,\phi}[n]\big)}, \tag{7}$$

where $\hat{m}_\phi[n]$ is the phasor-based estimate of the fault distance for the selected phase.

With $\hat{m}_\phi[n]$, the fault-point voltage phasor is obtained by back-substitution,

$$\hat{V}_{f,\phi}[n] = \hat{V}_{1,\phi}[n] - \hat{m}_\phi[n]\, Z_\ell\, \hat{I}_{1,\phi}[n]. \tag{8}$$

Define the fault current phasor as

$$\hat{I}_{f,\phi}[n] \triangleq \hat{I}_{1,\phi}[n] + \hat{I}_{2,\phi}[n], \tag{9}$$

where $\hat{I}_{f,\phi}[n]$ represents the total current flowing into the fault from both line terminals.

The fault resistance estimate follows from the real projection of the fault-loop relation,

$$\hat{R}_{f,\phi}[n] = \frac{\Re\left\{\hat{V}_{f,\phi}[n]\hat{I}^*_{f,\phi}[n]\right\}}{\left|\hat{I}_{f,\phi}[n]\right|^2}, \tag{10}$$

where $\hat{R}_{f,\phi}[n]$ is the estimated fault resistance, $\Re\{\cdot\}$ denotes the real part, $(\cdot)^*$ denotes complex conjugation, and $|\cdot|$ denotes the phasor magnitude.

C. Single-Ended Phasor Distance Protection Mechanism

A conventional single-ended distance element estimates an apparent impedance as

$$\hat{Z}_\phi[n] = \frac{\hat{V}_\phi[n]}{\hat{I}_\phi[n]}, \tag{11}$$

where $\hat{Z}_\phi[n]$ is the apparent impedance, and $\hat{V}_\phi[n]$ and $\hat{I}_\phi[n]$ are the local voltage and current phasors.

For phase-to-ground faults (e.g., a–G), a common compensated form is

$$\hat{Z}_{a\mathrm{G}}[n] = \frac{\hat{V}_a[n]}{\hat{I}_a[n] + k_0\,\hat{I}_0[n]}, \tag{12}$$

where $\hat{I}_0[n]$ is the zero-sequence current phasor, and k_0 is the zero-sequence compensation factor of the protected line.

Biased phasors propagate to apparent impedance through a ratio. Let $\hat{V} = V_1 + e_V$ and $\hat{I} = I_1 + e_I$, where V_1 and I_1 denote the (nominal-frequency) fundamental phasors and e_V, e_I collect estimation bias and distortion. Then

$$\hat{Z} = \frac{\hat{V}}{\hat{I}} = \frac{V_1}{I_1}\left(1 + \frac{e_V}{V_1} - \frac{e_I}{I_1}\right) + \mathcal{O}(e^2). \tag{13}$$

So small phasor errors can be strongly amplified when $|I_1|$ is small or rapidly varying, and also when $|V_1|$ becomes weak during severe voltage depression. This amplification can yield transient overreach/underreach and erratic R–X trajectories.

D. Phasor Directional Supervision

A phasor directional comparator forms a torque-like quantity from a polarizing voltage phasor and an operating current phasor. To avoid ill-conditioning during voltage depression, the polarizing voltage is selected by a simple magnitude logic. Let $\hat{V}_{\mathrm{mem}}$ be the memorized prefault polarizing phasor. Define

$$\hat{V}_{\mathrm{pol}}[n] \triangleq \begin{cases} \hat{V}_\phi[n], & \left|\hat{V}_\phi[n]\right| \geq \alpha_v \left|\hat{V}_{\mathrm{mem}}\right|, \\ \hat{V}_{\mathrm{mem}}, & \text{otherwise}, \end{cases} \tag{14}$$

where $\alpha_v \in (0, 1)$ is a voltage threshold.

The torque is then defined as

$$T[n] \triangleq \Re\left\{\hat{V}_{\mathrm{pol}}[n]\hat{I}^*_\phi[n]\right\}. \tag{15}$$

The sign of the torque provides the direction decision

$$\hat{d}[n] \triangleq \mathrm{sign}\big(T[n]\big) \in \{-1, +1\}. \tag{16}$$

IV. Geometric-Frequency-Based Protection Principles

A. Geometric Invariants and Short-Window Estimation

Three-phase voltages and currents are assumed to be the velocities of generalized trajectories in $\mathbb{R}^3$ [12]. The space is defined by the (a, b, c) phases of the transmission line and voltage and current vectors are assumed to be coordinates on a Cartesian basis $(\boldsymbol{e}_a, \boldsymbol{e}_b, \boldsymbol{e}_c)$. For example, considering the voltage vector:

$$\boldsymbol{u}(t) = u_a(t)\boldsymbol{e}_a + u_b(t)\boldsymbol{e}_b + u_c(t)\boldsymbol{e}_c, \tag{17}$$

or, equivalently:

$$\boldsymbol{u}(t) = [u_a(t), u_b(t), u_c(t)]^\top. \tag{18}$$

The geometric-frequency descriptors separate amplitude modulation from rotational motion [32]:

$$\rho_u(t) = \frac{\boldsymbol{u}(t)\cdot\boldsymbol{u}'(t)}{\|\boldsymbol{u}(t)\|^2}, \qquad \boldsymbol{\omega}_u(t) = \frac{\boldsymbol{u}(t)\times\boldsymbol{u}'(t)}{\|\boldsymbol{u}(t)\|^2}, \tag{19}$$

where $\cdot$ and $\times$ indicate the inner and cross product, respectively; and $\|\boldsymbol{u}\|$ indicates the Euclidean norm, namely $\|\boldsymbol{u}\| = \sqrt{\boldsymbol{u}\cdot\boldsymbol{u}}$. The inner product returns a scalar and represents the projection of a vector onto another vector. Considering two generic vectors $\boldsymbol{a}$ and $\boldsymbol{b}$ in $\mathbb{R}^n$, the inner product is given by:

$$\boldsymbol{a}\cdot\boldsymbol{b} = \boldsymbol{a}^\top\boldsymbol{b} = \sum_{k=1}^{n} a_k b_k\,. \tag{20}$$

The cross product is defined only in $\mathbb{R}^3$ and returns a vector perpendicular to the input vectors. It can be calculated as the determinant of the following matrix:

$$\boldsymbol{a}\times\boldsymbol{b} = \begin{vmatrix} \boldsymbol{e}_1 & \boldsymbol{e}_2 & \boldsymbol{e}_3 \\ a_1 & a_2 & a_3 \\ b_1 & b_2 & b_3 \end{vmatrix}, \tag{21}$$

where $(\boldsymbol{e}_1, \boldsymbol{e}_2, \boldsymbol{e}_3)$ are unit vectors of a Cartesian basis.

Reference [32] proves that ρ and $\boldsymbol{\omega}$ satisfy the identity:

$$\boldsymbol{u}'(t) = \rho_u(t)\,\boldsymbol{u}(t) + \boldsymbol{\omega}_u(t)\times\boldsymbol{u}(t) = \tilde{\boldsymbol{\Gamma}}_u\,\boldsymbol{u}, \tag{22}$$

where $\tilde{\boldsymbol{\Gamma}}_u$ is the geometric frequency of the voltage vector. A similar expression can be obtained for the time derivative of the current vector:

$$\boldsymbol{\imath}'(t) = \rho_\imath(t)\,\boldsymbol{\imath}(t) + \boldsymbol{\omega}_\imath(t)\times\boldsymbol{\imath}(t) = \tilde{\boldsymbol{\Gamma}}_\imath\,\boldsymbol{\imath}. \tag{23}$$

Fig. 3 illustrates that ρ_u captures the instantaneous radial stretching of the three-phase vector $\boldsymbol{u}$. The angular-velocity vector $\boldsymbol{\omega}_u$ specifies the instantaneous rotation axis through its direction and the rotation sense by the right-hand rule. Accordingly, geometric frequency characterizes, in real time, both the frequency axis given by the orientation of $\boldsymbol{\omega}_u$ and the rotational speed given by $\|\boldsymbol{\omega}_u\|$.

It is important to note that the quantities ρ and $\|\boldsymbol{\omega}\|$ are geometric invariants, that is, their value is independent from the coordinates that are utilized to define the "velocity" vectors. For example, the values of ρ and $\|\boldsymbol{\omega}\|$ do not change if voltage (or current) vectors are transformed from (a, b, c) to Clarke (α, β, γ) or Park (d, q, o) coordinates.

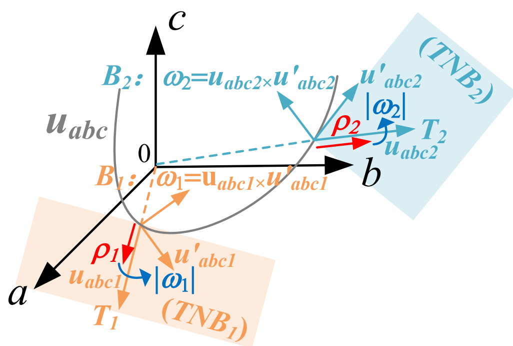

Fig. 3. Geometric frequency interpretation.

Note that, for relay implementation, derivatives are obtained via a short-window least-squares (LS) differentiator over the short window $\mathcal{W}_n$:

$$\boldsymbol{u}'[n] \approx \sum_{r=-K}^{K} c_r^{(1)}\, \boldsymbol{u}[n+r]. \tag{24}$$

After the LS coefficients are fixed, derivative estimation can be implemented as a fixed-coefficient finite impulse response operation, and the remaining GF steps only involve fixed-dimensional three-phase vector operations with fixed per-sample computational burden.

B. Two-Ended GF Distance Protection with Fault Resistance

When synchronized two-ended measurements are available, the GF formulation can exploit both terminals to estimate the fault location m and the fault resistance R_f in a short window, without relying on cycle-based phasors.

Let synchronized measurements be $\{\boldsymbol{v}_1(t), \boldsymbol{\imath}_1(t)\}$ and $\{\boldsymbol{v}_2(t), \boldsymbol{\imath}_2(t)\}$. For each terminal current,

$$\boldsymbol{\imath}_j'(t) = \tilde{\boldsymbol{\Gamma}}_{\imath_j} \boldsymbol{\imath}_j(t), \quad j \in \{1, 2\}. \tag{25}$$

Define the series-drop vectors

$$\boldsymbol{u}_j(t) = \big(R_\ell + L_\ell \tilde{\boldsymbol{\Gamma}}_{\imath_j}(t)\big)\boldsymbol{\imath}_j(t). \tag{26}$$

The two-ended KVL relations are

$$\boldsymbol{v}_1(t) = \boldsymbol{v}_f(t) + m\,\boldsymbol{u}_1(t), \boldsymbol{v}_2(t) = \boldsymbol{v}_f(t) + (1-m)\,\boldsymbol{u}_2(t). \tag{27}$$

Eliminating $\boldsymbol{v}_f(t)$ yields the linear-in-m relation

$$\boldsymbol{v}_1 - \boldsymbol{v}_2 + \boldsymbol{u}_2 = m\big(\boldsymbol{u}_1 + \boldsymbol{u}_2\big). \tag{28}$$

Define $\boldsymbol{a}[k] \triangleq \boldsymbol{u}_1[k] + \boldsymbol{u}_2[k]$ and $\boldsymbol{b}[k] \triangleq \boldsymbol{v}_1[k] - \boldsymbol{v}_2[k] + \boldsymbol{u}_2[k]$ over the window $\mathcal{W}_n$. When the windowed excitation satisfies $\sum_{k\in\mathcal{W}_n} \|\boldsymbol{a}[k]\|^2 > \epsilon_a$, with ϵ_a being a small positive threshold, the following least-squares estimate is adopted.

$$\hat{m}[n] = \frac{\sum\limits_{k\in\mathcal{W}_n} \boldsymbol{a}[k]^\top \boldsymbol{b}[k]}{\sum\limits_{k\in\mathcal{W}_n} \|\boldsymbol{a}[k]\|^2}. \tag{29}$$

Back-substitution gives $\hat{\boldsymbol{v}}_f[k]$, and with $\boldsymbol{\imath}_f[k] \triangleq \boldsymbol{\imath}_1[k] + \boldsymbol{\imath}_2[k]$, when the fault-current excitation satisfies $\sum_{k\in\mathcal{W}_n} \|\boldsymbol{\imath}_f[k]\|^2 > \epsilon_i$, with ϵ_i being a small positive threshold, the fault resistance can be estimated by projecting the fault-point voltage onto the fault current.

$$\hat{R}_f[n] = \frac{\sum\limits_{k\in\mathcal{W}_n} \hat{\boldsymbol{v}}_f[k]^\top \boldsymbol{\imath}_f[k]}{\sum\limits_{k\in\mathcal{W}_n} \|\boldsymbol{\imath}_f[k]\|^2}. \tag{30}$$

Physically, $\hat{m}$ represents the fraction of the protected-line series voltage drop between terminal 1 and the fault point, while $\hat{R}_f$ represents the resistive component seen at the fault point after the line drop is removed. Compared with the phasor-based two-ended formulation, the meanings of m and R_f remain unchanged; the key difference is that the input voltage-drop quantities $\boldsymbol{u}_1$ and $\boldsymbol{u}_2$ are extracted from instantaneous three-phase measurements through the GF-based R–L relation, rather than from cycle-based phasors.

C. Single-Ended GF Distance Protection and Fault Resistance Estimation

When communication or synchronization is unavailable, a single-ended element must rely on local voltage and current only. The GF formulation works directly with instantaneous three-phase trajectories and rewrites the current derivative through the GF kinematic matrix, enabling short-window estimates of distance and fault resistance.

For single-ended protection at terminal 1, neglecting the remote infeed current for the impedance calculation, the local fault-loop relation is modeled in a component-wise matrix form as

$$\boldsymbol{v}_1(t) \approx \mathbf{R}_d\, \boldsymbol{\imath}_1(t) + \mathbf{L}_d\, \boldsymbol{\imath}_1'(t), \tag{31}$$

where

$$\mathbf{R}_d \triangleq R_\ell \mathbf{M} + \mathbf{R}_f, \qquad \mathbf{L}_d \triangleq L_\ell \mathbf{M}. \tag{32}$$

Here, $\mathbf{M} = \mathrm{diag}(m_a, m_b, m_c)$ is the phase-dependent distance matrix, and $\mathbf{R}_f = \mathrm{diag}(R_{f,a}, R_{f,b}, R_{f,c})$ is the phase-dependent fault-resistance matrix.

Using GF kinematics, the series drop admits the equivalent R–L representation

$$\boldsymbol{v}_1(t) \approx \Big(\mathbf{R}_d + \mathbf{L}_d \widetilde{\boldsymbol{\Gamma}}_{\imath_1}(t)\Big)\, \boldsymbol{\imath}_1(t), \tag{33}$$

For the selected phase or fault-loop channel ϕ, taking the ϕ-component gives

$$v_{1,\phi}(t) \approx R_{d,\phi} \imath_{1,\phi}(t) + L_{d,\phi} \Big[\widetilde{\boldsymbol{\Gamma}}_{\imath_1}(t) \boldsymbol{\imath}_1(t)\Big]_\phi . \tag{34}$$

Over the short window $\mathcal{W}_n$, define

$$q_{1,\phi}[k] \triangleq \Big[\widetilde{\boldsymbol{\Gamma}}_{\imath_1}[k] \boldsymbol{\imath}_1[k]\Big]_\phi . \tag{35}$$

Define

$$\boldsymbol{\theta}_\phi[n] \triangleq \begin{bmatrix} R_{d,\phi}[n] \\ L_{d,\phi}[n] \end{bmatrix}, \qquad \boldsymbol{x}_\phi[k] \triangleq \begin{bmatrix} \imath_{1,\phi}[k] \\ q_{1,\phi}[k] \end{bmatrix}. \tag{36}$$

When the matrix inverse exists, the phase-dependent resistive and inductive components are estimated as

$$\hat{\boldsymbol{\theta}}_\phi[n] = \left(\sum_{k\in\mathcal{W}_n} \boldsymbol{x}_\phi[k] \boldsymbol{x}_\phi^\top[k]\right)^{-1} \sum_{k\in\mathcal{W}_n} \boldsymbol{x}_\phi[k] v_{1,\phi}[k], \tag{37}$$

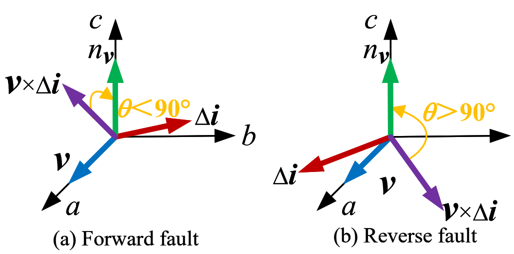

Fig. 4. Geometric-frequency directional principle.

where $\hat{\boldsymbol{\theta}}_\phi[n] = [\hat{R}_{d,\phi}[n], \hat{L}_{d,\phi}[n]]^\top$.

If a balanced three-phase disturbance is identified, the phase-dependent matrices in (31) can be further reduced to scalar equivalent parameters.

Taking dot and cross products of (33) with $\boldsymbol{\imath}_1(t)$ gives

$$\boldsymbol{v}_1 \cdot \boldsymbol{\imath}_1 \ = \big(R_d + L_d\rho_{i_1}\big)\|\boldsymbol{\imath}_1\|^2, \tag{38}$$
$$\boldsymbol{\imath}_1 \times \boldsymbol{v}_1 = L_d\|\boldsymbol{\imath}_1\|^2\boldsymbol{\omega}_{i_1}. \tag{39}$$

Therefore, the scalar inductive and resistive components can be obtained as

$$\hat{L}_{d,\phi}(t) = \frac{\boldsymbol{\omega}_{i_1}\cdot\big(\boldsymbol{\imath}_1\times\boldsymbol{v}_1\big)}{\|\boldsymbol{\imath}_1\|^2\|\boldsymbol{\omega}_{i_1}\|^2}, \quad \hat{R}_{d,\phi}(t) = \frac{\boldsymbol{v}_1\cdot\boldsymbol{\imath}_1}{\|\boldsymbol{\imath}_1\|^2} - \rho_{i_1}(t)\hat{L}_{d,\phi}(t). \tag{40}$$

With known line parameters (R_ℓ, L_ℓ), the phase-dependent distance and fault-resistance estimates are

$$\hat{m}_\phi = \frac{\hat{L}_{d,\phi}}{L_\ell}, \qquad \hat{R}_{f,\phi} = \hat{R}_{d,\phi} - \hat{m}_\phi R_\ell. \tag{41}$$

D. GF Directional Discrimination via Memory-Axis Projection

The GF directional element forms a torque-like quantity from instantaneous three-phase vectors and applies the same polarizing-voltage selection principle as phasor implementations. Let $\boldsymbol{v}[n]$ be the instantaneous three-phase voltage vector and $\boldsymbol{v}_{\text{mem}}$ be the memorized prefault polarizing voltage vector. The polarizing voltage vector is selected as

$$\boldsymbol{v}_{\text{pol}}[n] \triangleq \begin{cases} \boldsymbol{v}[n], & \|\boldsymbol{v}[n]\| \geq \alpha_v\|\boldsymbol{v}_{\text{mem}}\|, \\ \boldsymbol{v}_{\text{mem}}, & \text{otherwise}, \end{cases} \tag{42}$$

where $\alpha_v \in (0,1)$ is a voltage threshold.

Define the superimposed current as

$$\Delta\boldsymbol{\imath}[n] \triangleq \boldsymbol{\imath}[n] - \boldsymbol{\imath}_{\text{prefault}}[n]. \tag{43}$$

Then the torque-like vector is formed by the cross product

$$\boldsymbol{T}_{\text{GF}}[n] \triangleq \boldsymbol{v}_{\text{pol}}[n] \times \Delta\boldsymbol{\imath}[n]. \tag{44}$$

With a hemisphere-locked memory axis $\hat{\boldsymbol{n}}_{\text{mem}}$, the scalar torque and the direction decision are

$$\begin{aligned} T_{\text{GF}}[n] &\triangleq \hat{\boldsymbol{n}}_{\text{mem}}^\top \boldsymbol{T}_{\text{GF}}[n], \\ \hat{d}_{\text{GF}}[n] &\triangleq \text{sign}\big(T_{\text{GF}}[n]\big) \in \{-1,+1\}. \end{aligned} \tag{45}$$

Fig. 4 illustrates the physical meaning of the proposed directional criterion. The polarizing voltage vector provides the reference, and the superimposed current vector represents the fault-induced current change. Their cross product gives the rotation sense in the three-phase space, and the projection onto $\hat{\boldsymbol{n}}_{\text{mem}}$ converts this rotation into a signed scalar torque. In this way, the proposed criterion keeps the familiar forward or reverse interpretation of a memory-polarized directional element, while obtaining the sign directly from instantaneous three-phase vectors instead of full-cycle phasors.

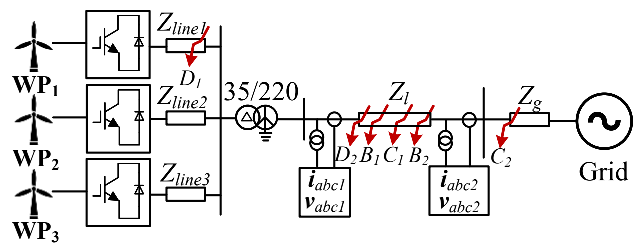

Fig. 5. Wind-farm export corridor used in EMT case studies.

TABLE II
MAIN CIRCUIT PARAMETERS OF THE WIND-FARM EXPORT CORRIDOR

Symbol	Meaning	Value
V_g	Grid voltage	220 kV
f_0	Nominal frequency	50 Hz
P_{WF}	Wind-farm rated active power (three units)	3×10 MW
n	Transformer turns ratio	35 kV / 220 kV
S_T	Transformer nominal apparent power	35 MVA
R_T	Transformer leakage resistance	0.016 pu
X_T	Transformer leakage reactance	0.06 pu
R_{line}	35 kV collection line resistance	0.4 Ω
L_{line}	35 kV collection line inductance	2.55 mH
ℓ	Length of protected line	100 km
Z_1/ℓ	Positive-sequence line impedance	$(0.03 + j0.34)$ Ω/km
Z_0/ℓ	Zero-sequence line impedance	$(0.18 + j1.19)$ Ω/km
Z_g	Grid impedance	$Z_g = j53.4$ Ω

V. Case Studies

A. Test System and Relay Settings

Fig. 5 shows the EMT test system: three identical 10 MW Type-4 converter-interfaced units are paralleled at a 35 kV collection bus and connected through a 35/220 kV step-up transformer to a 220 kV protected transmission line and a remote Thevenin grid. During the first post-fault interval, the converter-interfaced fault response may contain non-sinusoidal and nonstationary components due to current limiting, fast control transitions, and system-level nonlinear interactions. Therefore, the EMT cases include both near-sinusoidal and distorted fault-current responses to evaluate the robustness of the proposed method. The main circuit parameters are summarized in Table II.

Relay processing uses a reporting sampling rate of $f_s =$ 4 kHz, obtained by decimating EMT waveforms. Unless otherwise stated, GF estimates use a short window $T_{\text{GF}} =$ 3 ms, while the benchmark DFT element uses a full-cycle window $T_{\text{DFT}} = 20$ ms. The selected 3-ms window balances noise suppression and transient preservation, providing enough samples for LS-based differentiation without averaging out the fast post-fault waveform evolution.

TABLE III
EMT CASE SET AND STRESS CONDITIONS

Case	Function	Disturbance	m	R_f
B1	Two-ended distance	Three-phase fault	0.10	20
B2	Two-ended distance	A-to-ground fault	0.95	50
C1	Single-ended distance	A-to-ground fault	0.50	1.0
C2	Single-ended distance	Three-phase fault	1.20	0.1
D1	Directional	Three-phase fault, reverse	-0.05	5.0
D2	Directional	A-to-ground fault, forward	0.01	0.1

For GF locus plots, the reported impedance is mapped to nominal frequency:

$$\hat{Z}^{\mathrm{GF}}[n] \triangleq \hat{R}_d[n] + j\omega_0 \hat{L}_d[n], \qquad \omega_0 = 2\pi f_0. \tag{46}$$

Directional supervision uses instantaneous polarization when the voltage magnitude is sufficiently large; under voltage collapse, memory polarization is applied to both DFT and GF for a fair comparison.

The EMT case set and associated stress conditions are summarized in Table III. In what follows, we use these cases to validate the reliability of the proposed GF-based elements in three aspects: (i) two-ended distance and fault-resistance estimation (Cases B1–B2), (ii) single-ended distance and fault-resistance estimation (Cases C1–C2), and (iii) directional supervision under forward and reverse faults (Cases D1–D2). For all cases, the disturbance is applied at $t = 1.0$ s and cleared after 200 ms.

B. Two-Ended Distance Validation

This subsection validates two-ended distance and fault-resistance estimation using synchronized terminal data. To accommodate non-negligible fault resistance, a quadrilateral characteristic is adopted for distance setting; Zone 1 is set to cover 80% of the protected line, Zone 2 overreaches to 120%, and Zone 3 provides remote backup with a reach of 200%.

1) Case B1: internal three-phase fault

Case setup: an internal three-phase fault is applied at $m = 0.10$ with $R_f = 20\ \Omega$.

Fig. 6 reports the terminal voltages and currents together with their three-phase trajectories. The trajectories are close to planar, so the phasor assumption is reasonably valid and GF and DFT are expected to agree after the inception transient. Fig. 7 compares the time evolution of $\hat{m}$ and $\hat{R}_f$. Both methods converge to the correct fault location and fault resistance. GF reaches a stable result in about 5 ms, whereas DFT exhibits a damped transient and settles in about 30 ms. Fig. 8 shows the corresponding impedance locus and the zone boundaries. The GF locus contracts rapidly around the true point, while the DFT locus follows a longer transient spiral before converging.

Case B1 indicates that, under near-planar and near-sinusoidal conditions, both DFT and GF can accurately estimate the fault location and fault resistance and hence support the correct protection indication. However, the GF-based operating quantities settle noticeably faster than the DFT-based ones.

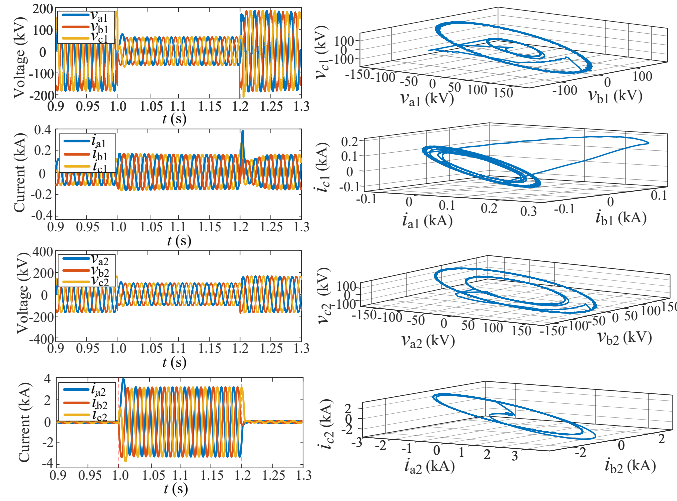

Fig. 6. Terminal waveforms in Case B1.

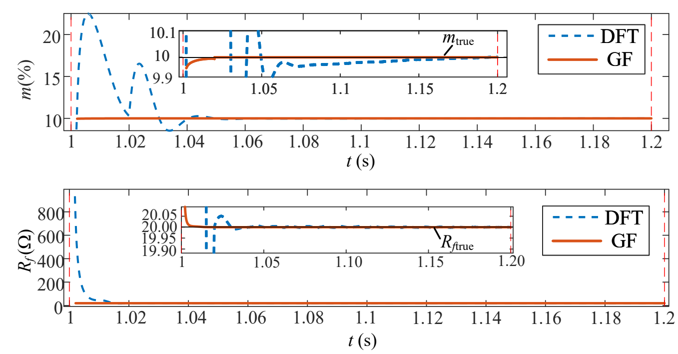

Fig. 7. Distance and fault resistance estimates in Case B1.

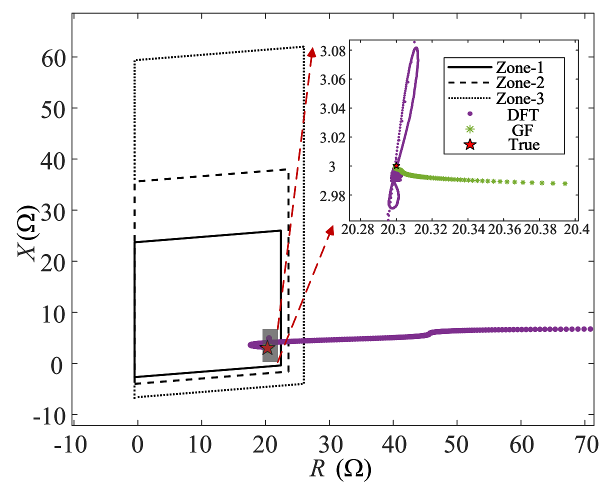

Fig. 8. Impedance locus in Case B1.

2) Case B2: internal A–G fault

Case setup: A far-end phase-A-to-ground fault is applied at $m = 0.95$ with $R_f = 50\ \Omega$. Under fault-induced system-level nonlinear effects, the phase-A current contains low-order harmonic distortion, including a third-harmonic component of 0.15 pu and a fifth-harmonic component of 0.10 pu

Fig. 9 reports the terminal waveforms and the corresponding three-phase trajectories. Compared with Case B1, the trajectories show clearer out-of-plane behavior, indicating that the post-fault waveforms deviate from a quasi-sinusoidal, strictly planar pattern during the early interval.

Fig. 10 compares the time evolution of $\hat{m}$ and $\hat{R}_f$. The GF-

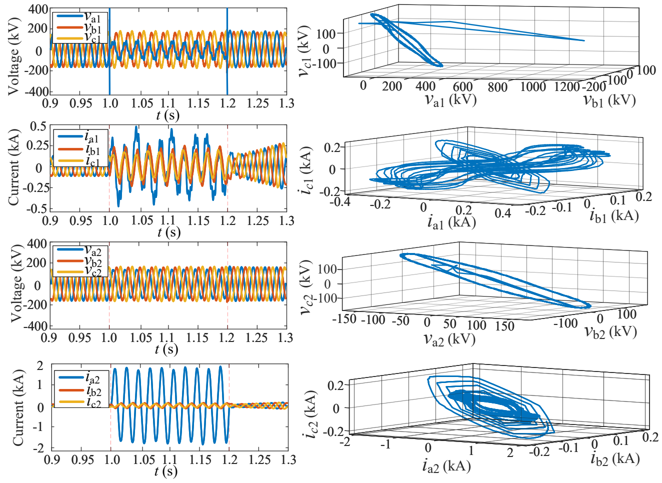

Fig. 9. Terminal waveforms in Case B2.

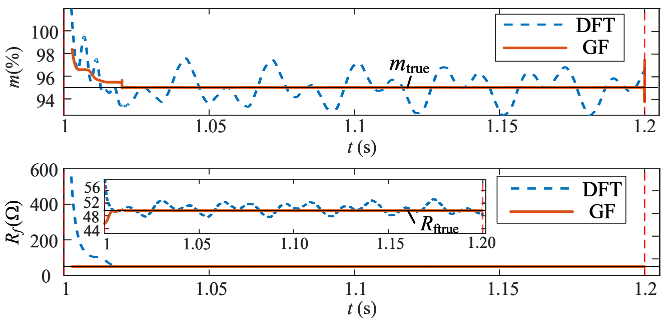

Fig. 10. Distance and fault resistance estimates in Case B2.

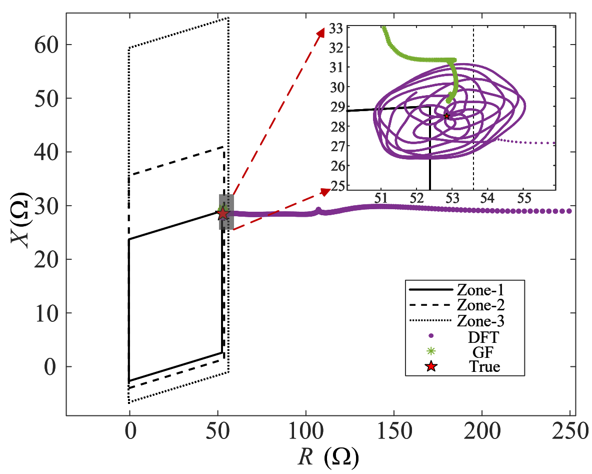

Fig. 11. Impedance locus in Case B2.

based estimates settle in about 10 ms and yield stable estimates of both fault location and fault resistance. By contrast, the DFT-based estimates exhibit larger transient oscillations and settle more slowly, with an approximate settling time of 38 ms and a residual distance-estimation error of about 4%.

Fig. 11 shows the corresponding impedance locus and the zone boundaries. The DFT locus presents larger excursions and can temporarily approach or cross incorrect regions, while the GF locus remains tighter and contracts rapidly around the true point, reducing the risk of transient zone misclassification.

Case B2 indicates that, under current limiting and low-order distortion with out-of-plane trajectory behavior, GF provides a faster-settling and more stable operating quantity than the cycle-based DFT benchmark.

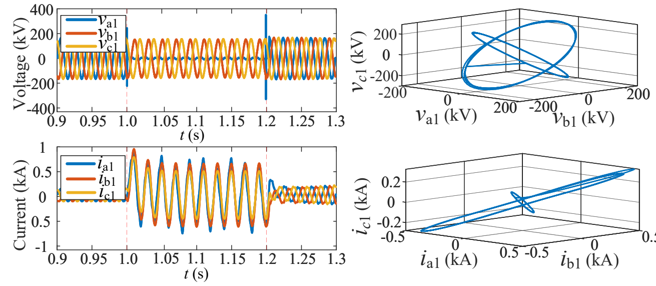

Fig. 12. Terminal waveforms in Case C1.

C. Single-Ended Distance Validation

This subsection evaluates distance and fault-resistance estimation using local measurements at terminal 1. For single-ended protection, the distance m and fault resistance R_f share the same resistive channel in the fault-loop model. As a result, when R_f is large, neither method can fully eliminate the intrinsic ambiguity without remote-terminal information. Therefore, Cases C1–C2 focus on mild-to-zero R_f so that the transient behavior and robustness of the operating quantities can be assessed. A mho characteristic is adopted as the benchmark single-ended operating region, and the corresponding loci are reported on the R–X plane for direct relay interpretation.

1) Case C1: internal phase-A-to-ground fault

Case setup: an internal A–G fault is applied at $m = 0.50$ with $R_f = 1\ \Omega$.

Fig. 12 reports the local terminal waveforms and the corresponding three-phase trajectories. The trajectories remain close to planar in this case, indicating that waveform nonplanarity is not the dominant difficulty. Fig. 13 compares the time evolution of $\hat{m}$ and $\hat{R}_f$. Both DFT and GF exhibit noticeable estimation bias and oscillation, which reflects the reduced identifiability of single-ended estimation under nonzero R_f.

GF shows smaller ripple and reaches a credible neighborhood of the true values in about 18 ms, while DFT exhibits larger oscillations and settles in about 45 ms. The corresponding distance-estimation errors are about 4% for GF and 10% for DFT.

Fig. 14 visualizes the impedance locus under the mho characteristic. The residual spread of the locus after settling indicates the intrinsic coupling between $\hat{m}$ and $\hat{R}_f$ in single-ended operation.

Case C1 indicates that, under single-ended measurement constraints, nonzero R_f unavoidably introduces bias because the relay cannot observe the remote-terminal current and the associated voltage drop on the fault resistance. In this regime, GF mainly improves the smoothness, distance-estimation accuracy, and early-time settling of the operating quantity compared with the cycle-based DFT benchmark.

2) Case C2: far-end three-phase external near-metallic fault with current waveform distortion

Case setup: An external far-end three-phase near-metallic fault is applied beyond the remote terminal, with equivalent $m = 1.20$ and $R_f = 0.1\ \Omega$. During the fault interval, the simulated fault current contains low-order harmonic distortion, with a third-harmonic current of approximately 0.10 pu and a fifth-harmonic current of approximately 0.20 pu of the fundamental component.

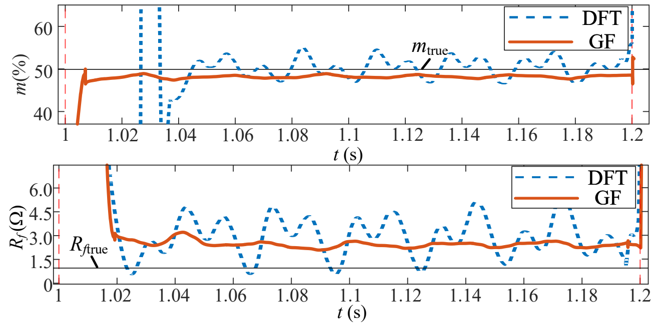

Fig. 13. Distance and fault resistance estimates in Case C1.

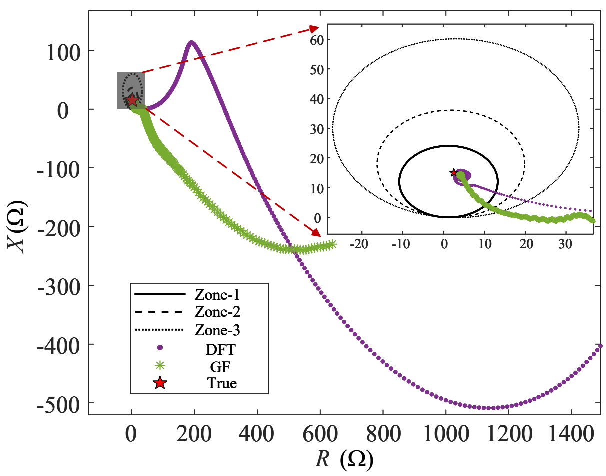

Fig. 14. Impedance locus in Case C1.

When R_f is close to zero, the line behavior is mainly governed by the series R–L channel. Therefore, the GF cross-product relation used to obtain $\hat{L}_d$ can reduce the influence of resistive coupling on the distance estimate $\hat{m}$.

Fig. 15 shows the local terminal waveforms and the corresponding three-phase trajectories. During the fault interval, the voltage and current waveforms are non-sinusoidal and nonstationary. The three-phase trajectories also deviate from a thin quasi-sinusoidal plane, which challenges cycle-based phasor estimation.

Fig. 16 compares the distance and fault-resistance estimates. After the initial transient, the GF-based distance estimate reaches a credible neighborhood of the expected value in about 20 ms, with a representative distance-estimation error of about 3%. Small residual ripples are still present. By contrast, the DFT-based estimates show larger sustained oscillations and do not satisfy the prescribed settling criterion before fault clearing. The representative DFT distance-estimation error is about 17%, and the oscillation is more evident in the fault-resistance channel.

Fig. 17 shows the impedance locus with the mho boundary. The DFT locus has a large transient excursion and a persistent oscillatory trajectory on the R–X plane. The GF locus is not completely stationary, but its post-transient points are more concentrated around the expected external-fault point.

Case C2 indicates that the GF-based result provides a more stable external-fault indication under the distorted-current condition.

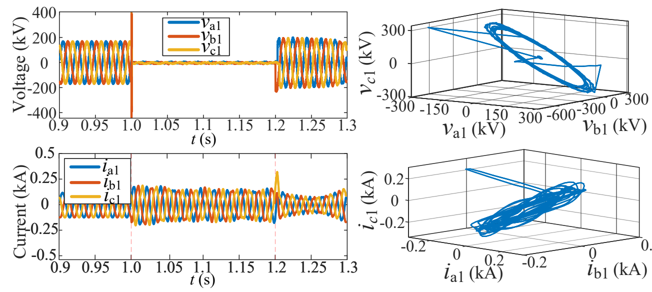

Fig. 15. Terminal waveforms in Case C2.

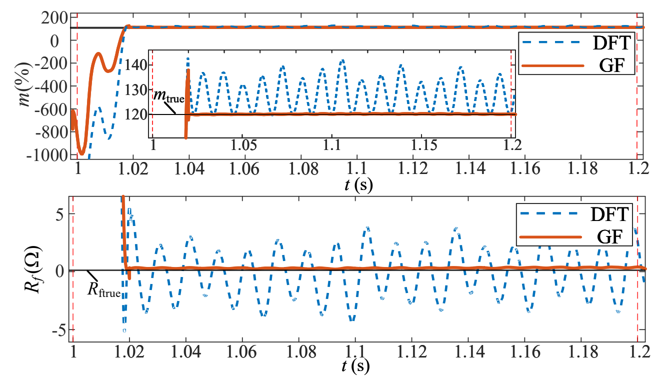

Fig. 16. Distance and fault resistance estimates in Case C2.

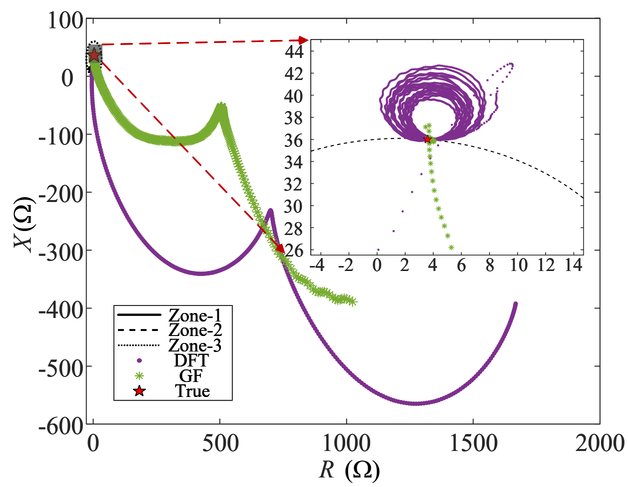

Fig. 17. Impedance locus in Case C2.

D. Directional Validation

This subsection compares directional criteria and their settling behavior for reverse and forward faults. The emphasis is placed on early-time sign stability, because directional supervision is often used to arm fast zones and block reverse faults.

1) Case D1: reverse fault with non-depressed voltage

Case setup: a reverse fault is applied with equivalent $m = -0.05$ and $R_f = 5\ \Omega$. Because the fault is electrically separated from the relay location by a transformer, the local voltage magnitude does not collapse and remains suitable for instantaneous polarization during the fault.

Fig. 19 reports the directional criterion and torque evolution. Both DFT and GF provide the correct reverse indication in this case. However, the GF-based directional criterion reaches a stable sign earlier because its operating quantity is formed from instantaneous three-phase geometry with a

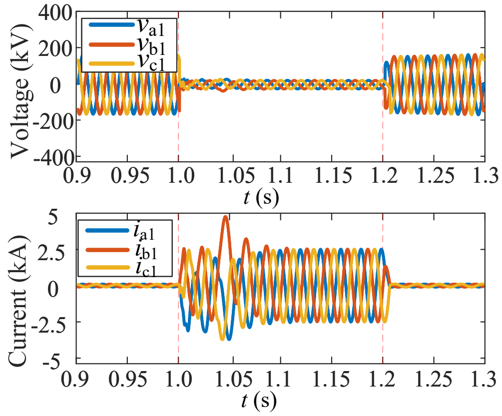

Fig. 18. Terminal waveforms in Case D1.

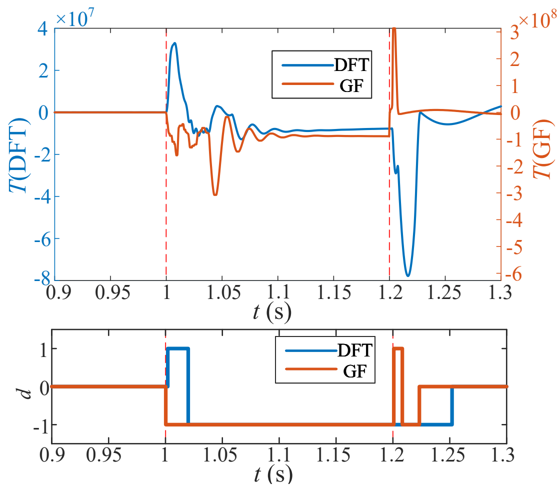

Fig. 19. Directional criteria in Case D1.

short window. With the settings used in this study, the GF-based criterion stabilizes in about 3 ms, while the DFT-based criterion requires about 20 ms to suppress the inception-driven fluctuation.

Case D1 indicates that, when voltage remains sufficiently large so that instantaneous polarization is well conditioned, both approaches are dependable, and the practical advantage of GF is the faster transition to a stable directional criterion.

2) Case D2: forward near-end A–G fault under voltage collapse

Case setup: a forward near-end phase-A-to-ground fault is applied at $m = 0.01$ with $R_f = 0.1\ \Omega$. In this case, the phase-A voltage drops close to zero after inception, so instantaneous polarization becomes ill conditioned and memory polarization is used for both methods.

Fig. 20 reports the terminal waveforms during the forward near-end fault. The phase-A voltage drops close to zero, confirming the voltage collapse condition. Fig. 21 reports the signed directional criterion. With memory polarization, both GF and DFT maintain a consistent forward directional sign. The GF-based criterion settles in about 10 ms, while the DFT-based criterion settles in about 14 ms.

The GF criterion remains responsive to the real-time current contribution and therefore stabilizes faster than the cycle-based DFT benchmark. This case also highlights a shared reliability

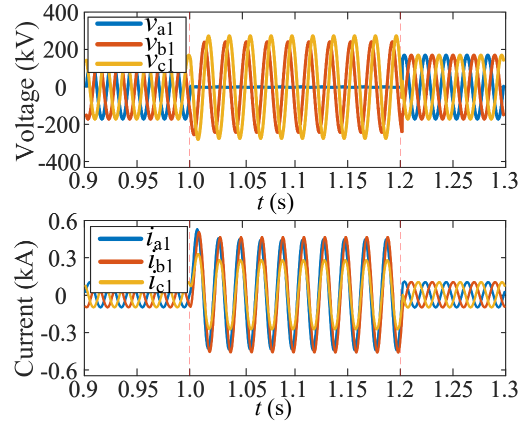

Fig. 20. Terminal waveforms in Case D2.

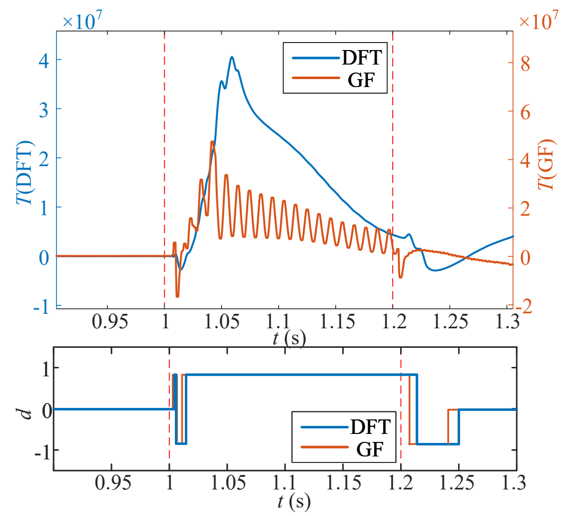

Fig. 21. Signed directional criterion in Case D2.

boundary of torque-comparator directional elements: the decision quality depends on a consistent relationship between the polarizing reference and the fault-driven current component. If a disturbance causes a large phase jump or a rapid rotation of the operating vectors, both methods can be stressed because the torque sign may temporarily lose its physical alignment.

Case D2 indicates that, under voltage collapse where memory polarization is required, GF preserves the same basic dependability as the phasor directional benchmark while providing a faster-settling directional criterion.

The representative settling-time and distance-estimation-error results from Cases B1–D2 are summarized in Table IV. As shown in Table IV, the GF-based operating quantities settle faster than the DFT-based benchmark in all tested EMT cases. For the distance cases, GF gives smaller distance-estimation errors, especially in Case C2 where the DFT estimate does not settle under severe waveform distortion. For the directional cases, the GF-based directional criterion also reaches a stable sign earlier than the DFT-based criterion.

E. Robustness to Measurement Imperfections

Since the proposed GF extractor uses short-window differentiation of instantaneous voltage and current measurements, its robustness is further tested under measurement noise, current transformer (CT) saturation, and communication delay. Three representative cases are selected: B2 for two-ended

TABLE IV
REPRESENTATIVE SETTLING-TIME AND RELATIVE DISTANCE-ESTIMATION-ERROR COMPARISON IN EMT CASES

Case	GF settling time (ms)	DFT settling time (ms)	GF relative distance error (%)	DFT relative distance error (%)
B1	5	30	0	0
B2	10	38	0	4
C1	18	45	4	10
C2	20	Not settled	3	17
D1	3	20	–	–
D2	10	14	–	–

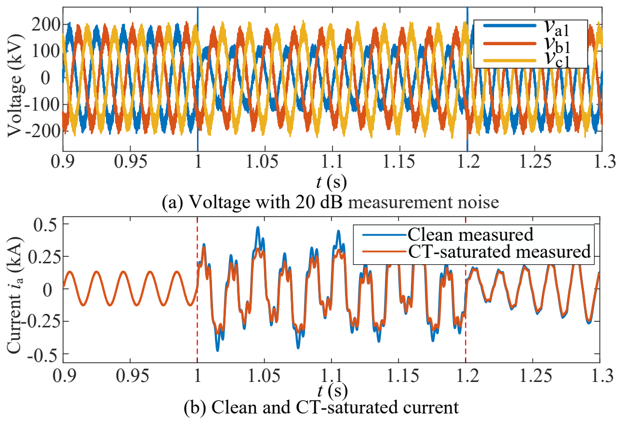

Fig. 22. Robustness-test waveforms of Case B2.

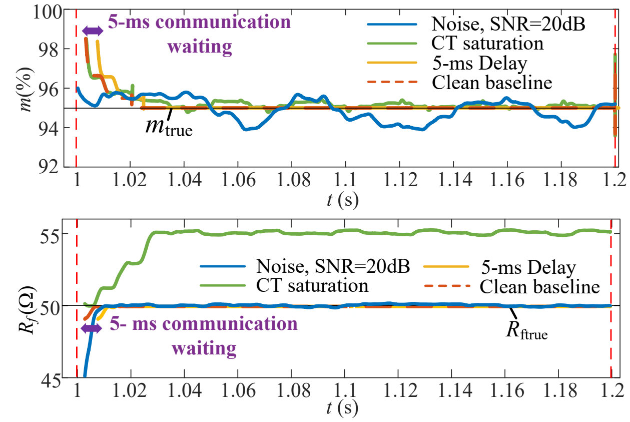

Fig. 23. Two-ended GF distance result of Case B2 under 20 dB measurement noise, CT saturation, and 5 ms communication waiting.

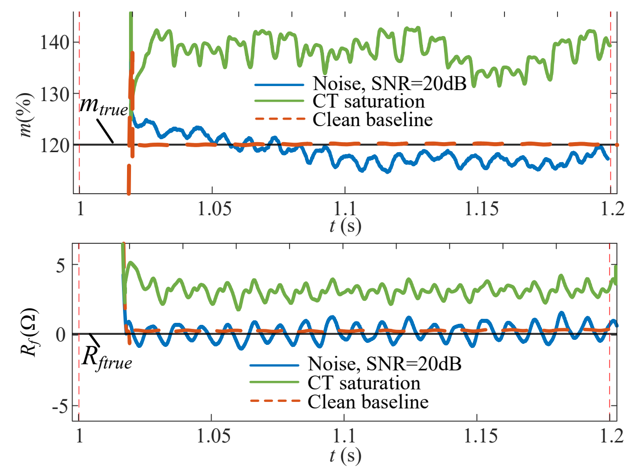

Fig. 24. Single-ended GF distance result of Case C2 under 20 dB measurement noise and CT saturation.

distance protection, C2 for single-ended distance protection, and D1 for single-ended directional protection.

For the noise test, additive white noise with a signal-to-noise ratio (SNR) of 20 dB is imposed on the measured signals. For the saturation test, CT saturation is imposed on the current measurement to emulate transducer-induced waveform distortion, while forced PT saturation is not imposed because the studied short-circuit disturbances mainly cause voltage depression. Fig. 22 shows the noisy voltage waveform and the CT-saturated current waveform of Case B2.

For the two-ended implementation, communication delay is considered by a 5 ms remote-data waiting strategy. The terminal data are aligned by time stamps, and the local and remote samples are selected from the same physical time window after the waiting interval. Therefore, this delay mainly affects the reporting time rather than the synchronization of the two-ended GF calculation.

The two-ended GF results of Case B2 are shown in Fig. 23. Under 20 dB noise, the estimated fault location and fault resistance remain close to the clean reference. CT saturation causes a more visible deviation in the estimated fault resistance because the current waveform is directly distorted. However, the estimated fault location remains close to the true value, and the final protection decision is still consistent with the clean reference.

Case C2 is used to examine the single-ended GF distance protection under local measurement imperfections. Since only local voltage and current measurements are used, no communication waiting is involved. As shown in Fig. 24, the 20 dB noisy-measurement case introduces visible fluctuations and a moderate bias in both $\hat{m}$ and $\hat{R}_f$ compared with the clean baseline. Nevertheless, the overall distance indication remains qualitatively consistent with the clean reference. CT saturation causes a larger deviation because the distorted current directly changes the local voltage-current relationship used by the single-ended GF extractor. Therefore, the single-ended element remains effective for the tested decision task, but its accuracy is more sensitive to local measurement distortion than the two-ended formulation.

Case D1 is used to examine the single-ended GF directional criterion under local measurement imperfections. The results are shown in Fig. 25. The GF directional quantity keeps the expected sign during the fault interval under both 20 dB noise and CT saturation, and the discrete directional decision remains consistent. After fault clearing, temporary fluctuations may appear due to waveform recovery and saturation distortion, but they do not affect the fault-period directional decision.

In summary, the added tests show that 20 dB measurement noise and the 5 ms communication waiting strategy have limited influence on the tested GF operating quantities. CT saturation has a stronger effect, especially for the single-ended distance result, but the fault-location indication and directional

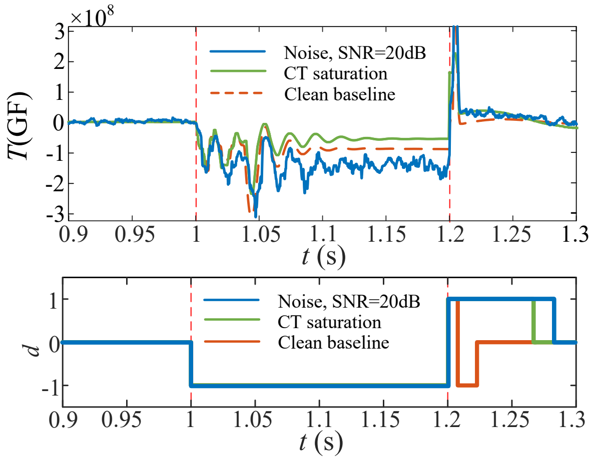

Fig. 25. Single-ended GF directional result of Case D1 under 20 dB measurement noise and CT saturation.

decision remain usable in the tested cases.

VI. Real-Time Experimental Validation

A. Test System

To further verify the practical feasibility of the proposed GF-based operating-quantity extraction, an RTDS-based real-time experimental validation is carried out.

The validation system is developed from the modified IEEE 9-bus benchmark in [33]. The main network parameters and converter parameters follow this benchmark. In this paper, the system is further modified to cover different types of generation resources and converter control strategies. Specifically, the test system contains one synchronous machine, one grid-forming converter with virtual synchronous generator control, and one grid-following converter with droop control. Both converter-based resources are equipped with low-voltage ride-through and current-limiting functions. Therefore, the test system includes mixed synchronous-machine, grid-forming-converter, and grid-following-converter dynamics, as shown in Fig. 26.

The protected line is the transmission line between Bus 8 and Bus 9. The three-phase voltages at Buses 8 and 9 and the branch currents of Line 8–9 are measured for two-ended distance protection, single-ended distance protection, and memory-polarized directional protection. Fig. 27 shows the RTDS experimental platform. The modified IEEE 9-bus system is implemented in the real-time simulator, and the measured three-phase voltage and current signals are used by the DFT-based and GF-based algorithms to calculate the corresponding distance and directional operating quantities. For all cases, the disturbance is applied at $t = 10.0$ s and cleared at $t = 10.2$ s.

B. Case R1: Three-Phase Disturbance

Case setup: A forward three-phase-to-ground fault is applied on the protected line close to Bus 8. The fault location is set to $m = 5\%$, and the fault resistance is set to $R_f = 5\ \Omega$. This case is used to verify the two-ended distance element, the single-ended distance element, and the memory-polarized

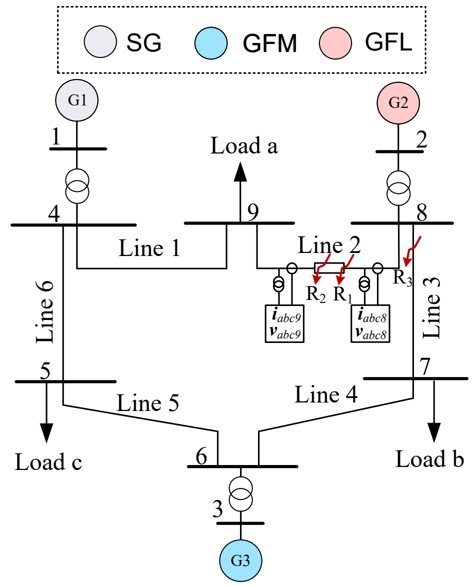

Fig. 26. Modified IEEE 9-bus test system.

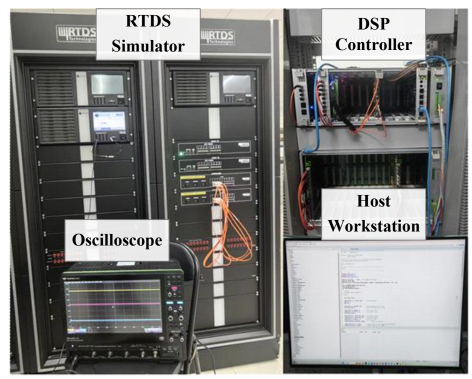

Fig. 27. RTDS experimental platform.

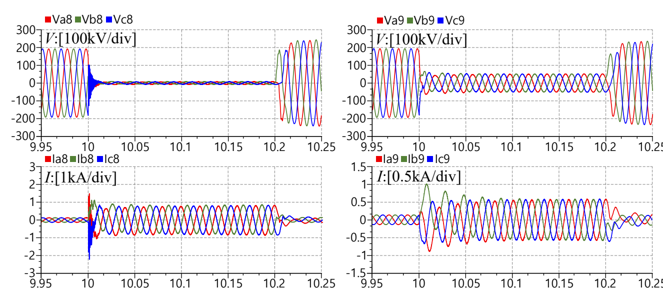

Fig. 28. Terminal waveforms in Case R1.

directional element under an internal balanced fault. Both DFT-based and GF-based operating quantities are calculated for comparison.

Fig. 28 shows the measured three-phase voltages and currents under the forward three-phase fault. The three-phase voltage and current signals exhibit clear fault-induced transient variations. Fig. 29 shows the corresponding protection results. For the two-ended distance element, the GF-based estimate correctly indicates the internal fault location and gives a stable fault-resistance estimate. For the single-ended distance element, the GF-based impedance-related quantity also enters the operating region and remains stable after the initial transient.

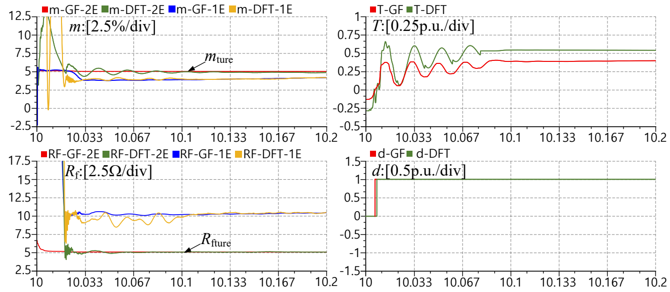

Fig. 29. Distance and directional protection results in Case R1.

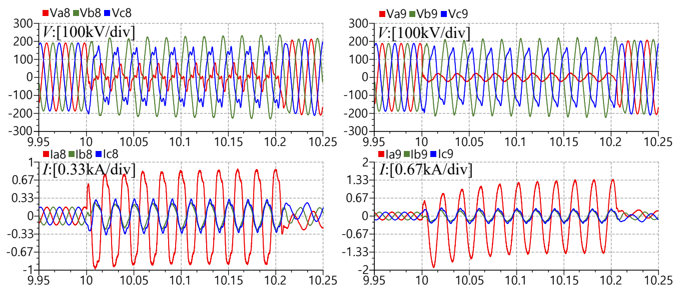

Fig. 30. Terminal waveforms in Case R2.

The DFT-based benchmark can also provide the correct final indication, but its operating quantities exhibit a longer transient process because of the full-cycle phasor window. For the directional element, the GF-based torque gives the correct forward indication and reaches a stable sign earlier than the DFT-based benchmark.

C. Case R2: Phase-A-to-Ground Disturbance

Case setup: A forward phase-A-to-ground fault is applied on the protected line near the remote end. The fault location is set to $m = 80\%$, and the fault resistance is set to $R_f = 0.5\ \Omega$. This case is used to verify the proposed method under an unbalanced single-phase fault condition. The two-ended distance element, single-ended distance element, and directional element are all tested, and the DFT-based results are used as the benchmark for comparison.

Fig. 30 shows the unbalanced voltage and current responses caused by the phase-A-to-ground fault. Fig. 31 shows the corresponding protection results. The GF-based two-ended distance element correctly identifies the internal fault and provides stable estimates of the fault location and fault resistance. The single-ended GF-based quantity also gives a consistent internal-fault indication using only local measurements. Compared with the DFT-based benchmark, the GF-based quantities settle faster because the derivative and geometric-frequency quantities are extracted over a short data window rather than a full-cycle phasor window. The directional result also remains forward, showing that the proposed memory-polarized directional element can operate correctly under an unbalanced single-phase disturbance.

D. Case R3: Reverse Disturbance

Case setup: A reverse disturbance is applied behind Bus 8. The equivalent location is set to $m = -10\%$, and the fault

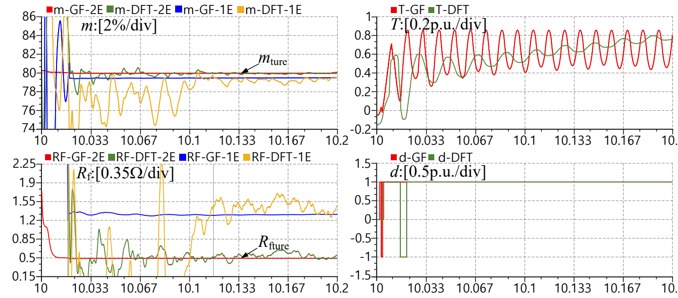

Fig. 31. Distance and directional protection results in Case R2.

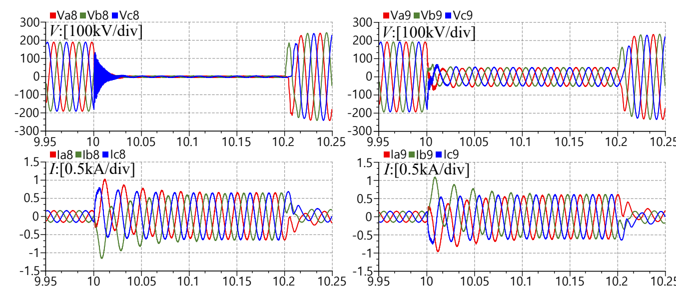

Fig. 32. Terminal waveforms in Case R3.

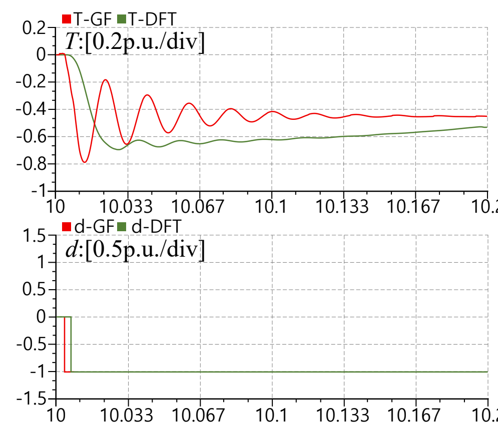

Fig. 33. Signed directional criterion in Case R3.

resistance is set to $R_f = 1\ \Omega$. This case is used to verify whether the proposed memory-polarized directional element can correctly identify a reverse disturbance and block forward tripping. The GF-based directional quantity is compared with the DFT-based directional benchmark.

Fig. 32 shows the measured voltage and current waveforms under the reverse disturbance. Fig. 33 shows the directional protection results. Both GF-based and DFT-based directional quantities indicate the reverse direction, confirming that the disturbance should be blocked by the forward directional element. Compared with the DFT-based benchmark, the GF-based directional torque gives a clearer negative indication during the early transient stage because it is constructed directly from instantaneous three-phase vectors and memory-axis projection. Therefore, this case verifies that the proposed directional element can correctly identify a reverse disturbance and avoid an incorrect forward trip.

Table V summarizes the RTDS validation results in terms

TABLE V
REPRESENTATIVE SETTLING-TIME, DECISION, AND RELATIVE DISTANCE-ESTIMATION-ERROR COMPARISON IN RTDS CASES

Case	Element	GF settling time (ms)	DFT settling time (ms)	GF decision	DFT decision	GF relative distance error (%)	DFT relative distance error (%)
R1	Two-ended distance	5	20	Internal	Internal	0	2
	Single-ended distance	20	30	Internal	Internal	25	28
	Directional	8	10	Forward	Forward	–	–
R2	Two-ended distance	5	24	Internal	Internal	0	0.15
	Single-ended distance	18	Not settled	Internal	Internal	0.84	5
	Directional	5	20	Forward	Forward	–	–
R3	Directional	5	7	Reverse	Reverse	–	–

of settling time, final decision, and relative distance-estimation error.

As shown in Table V, the GF-based elements give correct final decisions in all RTDS cases, and the DFT-based benchmark gives the same final decision except that the single-ended DFT quantity in Case R2 does not satisfy the settling criterion. In Cases R1 and R2, the two-ended and single-ended distance elements identify the forward faults as internal faults, and the directional element gives the correct forward indication. In Case R3, the directional element gives the correct reverse indication and blocks forward tripping.

Compared with the DFT-based benchmark, the GF-based quantities generally settle faster. Specifically, the two-ended GF distance element settles within 5 ms in Cases R1 and R2, while the corresponding DFT-based element requires 20 to 24 ms. The single-ended GF distance element also settles faster, requiring 20 ms in Case R1 and 18 ms in Case R2, whereas the DFT-based single-ended element requires 30 ms in Case R1 and does not settle in Case R2. The GF-based directional criterion settles within 5 to 8 ms in the tested RTDS cases.

The larger single-ended distance errors in Case R1 indicate the remaining accuracy limitation of local-only distance estimation, but the internal-fault decision is still retained. Overall, these RTDS results verify that the proposed GF-based operating quantities can be extracted in a real-time digital simulation environment and interfaced with conventional distance and directional relay logic without changing the final decision characteristics.

VII. CONCLUSIONS

This paper develops a GF protection framework for the early post-fault interval in converter-dominated grids, where measured waveforms can be nonstationary and distorted. By treating three-phase quantities as trajectories in $\mathbb{R}^3$, the proposed method constructs relay operating quantities directly from instantaneous geometry, reducing dependence on cycle-based DFT phasors and their finite-window bias.

Based on the GF kinematic identity, waveform-consistent R–L representations are derived for distance and directional protection. In the two-ended setting, synchronized terminal measurements enable short-window estimation of the fault location $\hat{m}$ and fault resistance $\hat{R}_f$. In the single-ended setting, inner- and cross-product identities separate resistive and inductive channels using local measurements only. For directional supervision, memory-voltage and memory-axis projection provide a stable sign reference under voltage depression.

EMT studies show that both DFT and GF provide correct final indications under near-sinusoidal conditions, while the GF-based quantities settle faster. Under current limiting and low-order distortion, GF produces more stable operating quantities and tighter impedance loci. In the tested cases, the GF-based distance quantities settle within 5 to 20 ms, and the GF-based directional criteria stabilize within 3 to 10 ms. RTDS tests on a modified IEEE 9-bus transmission system further verify that the proposed two-ended distance, single-ended distance, and memory-polarized directional elements give correct indications for forward three-phase faults, forward phase-A-to-ground faults, and reverse disturbances.

The main limitation appears in the single-ended setting, where the coupling between m and R_f can reduce fault-resistance accuracy under transition resistance. Nevertheless, the inductive channel remains more separable, so the location estimate can still be dependable when the underlying series R–L relation is well satisfied. Future work will investigate prototype relay implementation, further validate the method, and extend GF-based operating quantities to other protection functions in IBR-rich transmission systems, including ROCOF-based protection.

REFERENCES

[1] J. L. Blackburn and T. J. Domin, *Protective Relaying: Principles and Applications*, 4th ed. Boca Raton, FL, USA: CRC Press, 2014.
[2] *IEEE Guide for Protective Relay Applications to Transmission Lines*, IEEE Std. IEEE Std C37.113-2015, 2015.
[3] A. G. Phadke and J. S. Thorp, *Computer Relaying for Power Systems*, 2nd ed. Hoboken, NJ, USA: Wiley, 2009.
[4] IEEE Power System Relaying and Control Committee (PSRCC), Working Group C32, "Protection challenges and practices for interconnecting inverter based resources to utility transmission systems," IEEE Power & Energy Society, Tech. Rep. PES-TR81, 2020.
[5] E. Chowdhury and N. Fischer, "Transmission line protection for systems with inverter-based resources— Part I: Problems," *IEEE Transactions on Power Delivery*, vol. 36, no. 4, pp. 2416–2425, Aug. 2021.
[6] Etik Energy Pty Ltd, "Grid-forming and grid-following inverter fault current contribution," Australian Energy Market Operator, Independent Consultant Report, Nov. 2025, accessed: Jan. 24, 2026. [Online]. Available: https://www.aemo.com.au/-/media/files/initiatives/engineering-framework/2025/grid-forming-and-grid-following-inverter-fault-current-contribution.pdf
[7] M. Bini, R. Abboud, P. Lima, and F. Lollo, "Challenges and solutions in the protection of transmission lines connecting nonconventional power sources," in *Proc. 48th Annu. Western Protective Relaying Conf.*, Spokane, WA, USA, Oct. 2021, pp. 1–15.

[8] M. Nagpal, A. Saeed, R. Rangel, D. Zhang, and R. Chowdhury, "Fault contributions from inverter-based resources: Field insights and protection challenges," in *Proceedings of the 52nd Annual Western Protective Relay Conference*, Spokane, WA, USA, 2025.

[9] K. Jia, Z. Yang, Y. Fang, T. Bi, and M. Sumner, "Influence of inverter-interfaced renewable energy generators on directional relay and an improved scheme," *IEEE Transactions on Power Electronics*, vol. 34, no. 12, pp. 11 843–11 855, Dec. 2019.

[10] Y. Li, H. Wu, and X. Wang, "Challenges for distance relays in grid code-compliant inverter-based power systems: A review," *IEEE Open Journal of Power Electronics*, vol. 7, pp. 128–145, 2026.

[11] F. Milano, "Complex frequency," *IEEE Transactions on Power Systems*, vol. 37, no. 2, pp. 1230–1240, Mar. 2022.

[12] F. Milano, "A geometrical interpretation of frequency," *IEEE Transactions on Power Systems*, vol. 37, no. 1, pp. 816–819, Jan. 2022.

[13] F. Milano, G. Tzounas, I. Dassios, M. A. A. Murad, and T. Kërci, "Using differential geometry to revisit the paradoxes of the instantaneous frequency," *IEEE Open Access Journal of Power and Energy*, vol. 9, pp. 318–329, 2022.

[14] F. Milano, "The Frenet frame as a generalization of the Park transform," *IEEE Transactions on Circuits and Systems I: Regular Papers*, vol. 70, no. 2, pp. 966–976, Feb. 2023.

[15] S.-H. Kang, D.-G. Lee, S.-R. Nam, P. A. Crossley, and Y.-C. Kang, "Fourier transform-based modified phasor estimation method immune to the effect of the dc offsets," *IEEE Transactions on Power Delivery*, vol. 24, no. 3, pp. 1104–1111, Jul. 2009.

[16] A. Rahmati and R. Adhami, "An accurate filtering technique to mitigate transient decaying DC offset," *IEEE Transactions on Power Delivery*, vol. 29, no. 2, pp. 966–968, Apr. 2014.

[17] M. R. D. Zadeh and Z. Zhang, "A new DFT-based current phasor estimation for numerical protective relaying," *IEEE Transactions on Power Delivery*, vol. 28, no. 4, pp. 2172–2179, Oct. 2013.

[18] K. M. Silva and F. A. O. Nascimento, "Modified DFT-based phasor estimation algorithms for numerical relaying applications," *IEEE Transactions on Power Delivery*, vol. 33, no. 3, pp. 1165–1173, Jun. 2018.

[19] A. Banaiemoqadam, A. Hooshyar, and M. A. Azzouz, "A control-based solution for distance protection of lines connected to converter-interfaced sources during asymmetrical faults," *IEEE Transactions on Power Delivery*, vol. 35, no. 3, pp. 1455–1466, Jun. 2020.

[20] E. Chowdhury and N. Fischer, "Transmission line protection for systems with inverter-based resources—part II: Solutions," *IEEE Transactions on Power Delivery*, vol. 36, no. 4, pp. 2426–2433, Aug. 2021.

[21] A. Banaiemoqadam, A. Azizi, A. Hooshyar, M. Kanabar, and E. F. El-Saadany, "Impact of inverter-based resources on different implementation methods for distance relays—part i: Phase comparators," *IEEE Transactions on Power Delivery*, vol. 38, no. 6, pp. 4090–4102, Dec. 2023.

[22] H. Johansson, Q. Xing, N. Taylor, and X. Wang, "Impacts of grid-forming inverters on distance protection," *IET Generation, Transmission & Distribution*, vol. 19, no. 1, p. e13354, 2025.

[23] Y. Xie, X. Zou, M. Duan, F. Fan, H. Wang, and Y. Liu, "Distance protection for lines terminated by inverter-based resources compatible with various inverter control schemes," *IEEE Transactions on Industrial Electronics*, vol. 72, no. 12, pp. 13 151–13 163, Dec. 2025.

[24] I. E. O. Schweitzer, B. Kasztenny, A. Guzmán, V. Skendzic, and M. Mynam, "Speed of line protection—can we break free of phasor limitations?" in *Proceedings of the 68th Annual Conference for Protective Relay Engineers (CPRE)*, College Station, TX, USA, Apr. 2015, pp. 448–461.

[25] C. Zhang, J. Yan, L. Yang, J. Jiang, and G. Song, "Analysis of traveling wavefront information and wavefront protection for power electronic device-interfaced ac system," *IEEE Transactions on Power Delivery*, vol. 39, no. 1, pp. 407–425, Feb. 2024.

[26] C. Zhang, G. Song, and X. Dong, "Non-unit ultra-high-speed dc line protection method for hvdc grids using first peak time of voltage," *IEEE Transactions on Power Delivery*, vol. 36, no. 3, pp. 1683–1693, Jun. 2021.

[27] P. Jafarian and M. Sanaye-Pasand, "A traveling-wave-based protection technique using wavelet/pca analysis," *IEEE Transactions on Power Delivery*, vol. 25, no. 2, pp. 588–599, Apr. 2010.

[28] S. Sawai and A. K. Pradhan, "Travelling-wave-based protection of transmission line using single-end data," *IET Generation, Transmission & Distribution*, vol. 13, no. 20, pp. 4659–4666, 2019.

[29] B. Kasztenny, A. Guzmán, N. Fischer, M. V. Mynam, and D. Taylor, "Practical setting considerations for protective relays that use incremental quantities and traveling waves," in *Proceedings of the 43rd Annual Western Protective Relay Conference*, Spokane, WA, USA, Oct. 2016.

[30] A. Lei, X. Dong, and V. Terzija, "An ultra-high-speed directional relay based on correlation of incremental quantities," *IEEE Transactions on Power Delivery*, vol. 33, no. 6, pp. 2726–2735, Dec. 2018.

[31] Y. Chen, M. Wen, Z. Wang, X. Yin, and D. Chen, "An incremental quantities distance protection using park's transformation," *IEEE Transactions on Power Delivery*, vol. 37, no. 4, pp. 3200–3212, Aug. 2022.

[32] F. Milano, G. Tzounas, I. Dassios, and T. Kérci, "Applications of the Frenet frame to electric circuits," *IEEE Transactions on Circuits and Systems I: Regular Papers*, vol. 69, no. 4, pp. 1668–1680, Apr. 2022.

[33] A. Tayyebi, D. Groß, A. Anta, F. Kupzog, and F. Dörfler, "Frequency stability of synchronous machines and grid-forming power converters," *IEEE Journal of Emerging and Selected Topics in Power Electronics*, vol. 8, no. 2, pp. 1004–1018, 2020.